ADVANCED MATERIALS
www.advmat.de

Control Over Metal-Halide Reactivity Enables Uniform Growth of InSb Colloidal Quantum Dots for Enhanced SWIR Light Detection

*Muhammad Imran, Da Bin Kim, Pan Xia, Francisco Yarur Villanueva, Benjamin Rehl, Joao M. Pina, Yanjiang Liu, Yangning Zhang, Oleksandr Voznyy, Eugenia Kumacheva, Sjoerd Hoogland, and Edward H. Sargent**

InSb colloidal quantum dots (CQDs) hold promise in short-wave infrared sensing; however, their synthesis presents ongoing challenges, particularly in achieving precise size control – this is the result of poorly controlled reactivity among the precursors. Herein, the use of alkyl-phosphine and amine-based organic additives to control the reactivity of In and Sb precursors during the nucleation and growth of CQDs is developed. This interplay between organic additive and precursors enables the synthesis of InSb CQDs having narrowed size distributions; and bandgaps tunable across the 1.2–1.5 µm spectral range; all this leading to peak-to-valley ratios >1.4 in absorption spectra. The CQDs are surface-terminated with a mixture of oleylamine, halides, and oxide-like species, and this hinders ligand exchange reactions and subsequent integration into photodiodes. We therefore resurface the CQDs with alkanethiols, displacing the native ligands via an acid-base mechanism, an approach that removes oxide species. Using a layer-by-layer fabrication process, the ligands of the resurfaced InSb CQDs are exchanged with short organic and halide ligands and incorporated films into *n-i-p* photodiode structures. The resultant devices exhibit a detectivity of 10^{12} Jones, an external quantum efficiency (EQE) of 33% at 1380 nm, and T_{90} operating stability of >19 h under continuous illuminated operation.

1. Introduction

Shortwave infrared (SWIR) light offers potential for applications in optical communications, material identification, and imaging. Today's highest-performing SWIR detectors are based on III-V materials such as indium gallium arsenide (InGaAs), but reliance on epitaxial growth increases cost and makes these difficult to integrate with silicon CMOS electronics.[1] Thus, there is interest in new materials capable of converting photon signals into electrical current in this region of the spectrum.

Colloidal quantum dots (CQDs) are solution-processed, enabling monolithic integration with readout integrated circuits as a post-process.[2,3] Much CQD SWIR photodetection relies on lead, cadmium, and mercury-based CQDs, and these are subject to regulations such as the Restriction of Hazardous Substances (RoHS).[4]

Indium antimonide (InSb) is one III-V candidate; however, synthesizing high-quality InSb CQDs remains a challenge, often requiring pyrophoric and custom-synthesized antimony precursors.[5] Recent efforts to improve synthetic control have involved more stable indium and antimony precursors (tris(dimethylamido)antimony, metal silylamide, and $SbCl_3$).[6–9] Among those, commercially available and chemically stable metal halide precursors such as $InCl_3$ and $SbCl_3$ are of interest. These precursors have produced InSb CQDs with narrow size distributions for sizes up to 3 nm,

M. Imran, D. B. Kim, P. Xia, B. Rehl, J. M. Pina, Y. Zhang, S. Hoogland, E. H. Sargent
Department of Electrical and Computer Engineering
University of Toronto
10 King's College Road, Toronto, ON M5S 3G4, Canada
E-mail: ted.sargent@utoronto.ca

The ORCID identification number(s) for the author(s) of this article can be found under https://doi.org/10.1002/adma.202420273

DOI: 10.1002/adma.202420273

F. Y. Villanueva
Department of Chemistry
University of Toronto
80 St. George Street, Toronto, ON M5S 3H6, Canada

Y. Liu, O. Voznyy, E. Kumacheva
Department of Materials Science and Engineering
University of Toronto
184 College Street, Toronto, ON M5S 3E4, Canada

absorbing below 1200 nm with a peak-to-valley ratio of >1.2. Achieving a similar degree of size control for CQDs absorbing in the range of 1200–1500 nm with consistent reproducibility remains challenging. This is primarily due to uncontrolled reactivities of the In and Sb precursors.

An equally important challenge is the oxophilic nature of InSb, a feature that makes it prone to oxidation during both synthesis and post-synthesis CQD processing. This becomes even more important for larger InSb CQD particles, which are synthesized under In-rich conditions, leading to In-rich surfaces that are easily oxidized. Recent studies on III-V CQDs have shown that ligand exchanges using alkyl carboxylic acid, di-alkycaboxylic acid, alkane thiol, or a growing sub-nanometer shell of InP can effectively suppress the surface oxidation of InSb CQDs.[7,9–13] However, despite these synthetic advances, the performance of SWIR-active InSb CQD-based photodiodes remains limited, with EQEs so far <25%.

We hypothesized that enhanced control over the reactivity of the metal halide precursors could enable the growth of higher-quality InSb CQDs. Therefore, we sought to regulate the reactivity of metal halides using molecular additives. Using nuclear magnetic resonance (NMR) spectroscopy, we found that alkylphosphine/amine-based organic additives form strong adducts with $InCl_3$ and $SbCl_3$ precursors. These adducts regulate the In and Sb reactivity during nucleation and growth, enabling the controlled growth of InSb CQDs. As-synthesized InSb CQDs are surface terminated with a mixture of oleylamine, halides, and oxide-like species. We found that these ligands are labile and are prone to desorption during the purification process which hinders ligand exchange reactions, and consequently their integration as an active layer functional photodiode. We introduced alkanethiols to displace native ligands and oxides, thereby facilitating the ability to perform solid-state ligand exchanges to shorter organic-inorganic ligands and enabling the formation of homogeneous conductive films. This approach enabled us to fabricate highly efficient photodiodes, achieving an external quantum efficiency (EQE) of 33% at 1380 nm, a detectivity D^* of 10^{12} Jones, retaining 90% of their initial performance following 19 h of continuous illumination, surpassing all reported III-V CQDs-based SWIR photodetectors (see Table S1, Supporting Information, for the details).

2. Results and Discussion

In this study, we adapted the previously developed metal halide synthesis process with ZnX_2 additives, employed in the synthesis of InSb CQDs with bandgaps in ≈950–1200 nm wavelength range.[7] Detailed descriptions of the synthesis method and additional information can be found in the Materials and Methods section of Supporting Information. We aimed to further optimize reaction parameters to produce high-quality InSb CQDs with absorption in 1200–1500 nm range. In initial attempts, we controlled the reaction by varying the growth temperature and increasing the reaction time. However, the CQDs obtained from these reactions exhibited a featureless absorption spectrum (Figures S1 and S2, Supporting Information) and high-angle annular dark field scanning transmission electron microscopy (HAADF-STEM) analysis revealed CQDs with various shapes and a broad size distribution (Figure S3, Supporting Information). The lack of control over the growth of CQDs is a common challenge in the synthesis of high-quality large (>3.5 nm) In-pnictogenide CQDs, which is thought to be caused by the uncontrolled reactivities of the metal precursors.

We hypothesized that a quantitative, experimentally informed model of metal halide salt reactivity is essential to control the nucleation and growth of CQDs. To regulate the reactivity of these salts during nucleation and growth, we sought organic additives that bind strongly with metal halides. Previous studies on CQD synthesis have shown that organic complexation agents can stabilize precursors, influence growth kinetics, and improve size, shape control, and compositional uniformity.[10] We therefore explored the reactivities of organic additives with metal halide salts.

We explored a library of candidate organic additives, including di/tri-alkyl amines, alkyl phosphines, and alkyl phosphonic acids. In our reaction system, organic additives are expected to interact with either $InCl_3$ or $SbCl_3$, forming stable adducts and subsequently releasing precursors in a controlled manner at a desired reaction temperature.

To get mechanistic insight into the precursor chemistry of our system, we conducted NMR spectroscopy experiments. We focused on reactions employing trioctylphosphine (TOP) and OLAm as common organic additives in the synthesis of indium pnictogenides, allowing us to track the complexation of salts to the organics using ^{31}P and ^{1}H NMR (see details in Methods). We divided our experiments into four categories. The first two sets of experiments independently evaluated the behavior of indium and antimony precursors. Then, the third experiment aimed to track reaction intermediates and elucidate the overall process of precursor conversion into InSb CQDs while the fourth experiment was our control with a sterically hindered phosphine, triphenylphosphine (TPP).

We initially examined the interactions between $InCl_3$ and TOP in the presence of OLA. Our control experiments revealed a signal for free TOP organic at −32.22 ppm, unaffected by the addition of alane or OLAm (**Figure 1a** burgundy trace; Figure S4, Supporting Information). Therefore, any observed changes in peak shape and position can be attributed to interactions with $InCl_3$. Upon the addition of $InCl_3$, we observed a broadening and downfield shift of the TOP signal to −32.15 ppm, indicating a formal complexation between indium and TOP (Figure 1a). The ^{1}H NMR spectrum showed no broadening in the α-H of OLAm upon $InCl_3$ addition (Figures S5 and S6, Supporting Information), suggesting that OLAm remains uncomplexed. Introducing alane into the TOP-$InCl_3$-OLAm solution had minimal impact on the broad signal observed in the ^{31}P spectrum for the TOP-$InCl_3$ complex (Figure 1a), while the α-H signal for OLAm remained sharp (Figures S5 and S6, Supporting Information). This evidence suggests that indium preferentially complexes with TOP when both TOP and OLAm are present.

We then evaluated the interactions of $SbCl_3$ with TOP and OLAm. The ^{31}P NMR spectra revealed a downfield shift in the TOP signal upon $SbCl_3$ addition (Figure 1b). However, the signal broadening was less pronounced compared to the TOP-$InCl_3$ complex, suggesting a weaker interaction between TOP and $SbCl_3$. This is likely due to antimony's extra lone pair, which makes it sterically more hindered for complexation. Indeed, ^{1}H NMR showed significant broadening in the α-H of OLAm before the addition of alane, not observed with the indium

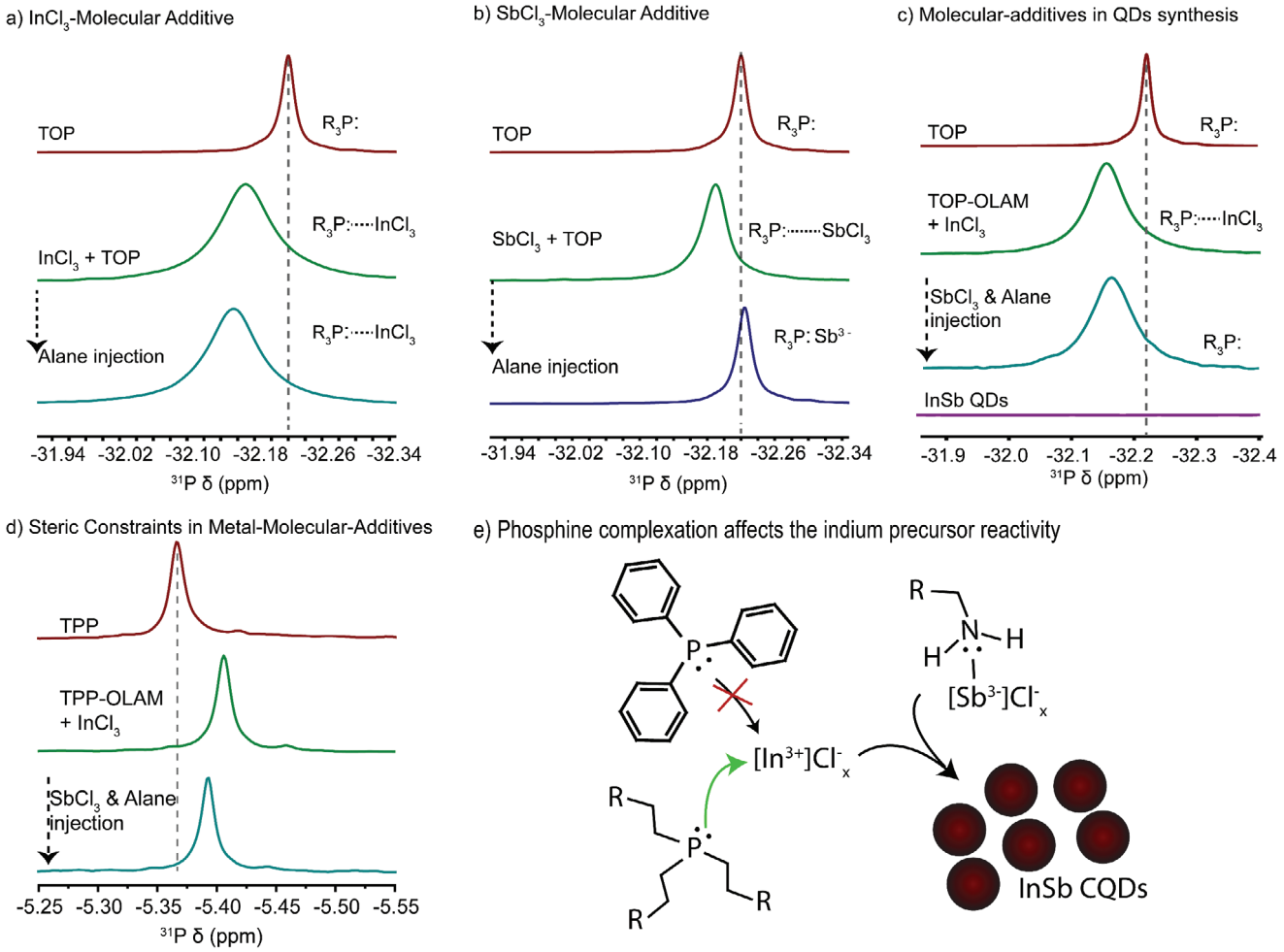

Figure 1. Regulating the reactivity of metal halides in the synthesis. ^{31}P NMR spectra in C_6D_6 for different organic additives found in the synthesis of InSb QDs. a) $InCl_3$-based organic additives: TOP complexes $InCl_3$ produce a downfield shift and broadening of the TOP signal. b) $SbCl_3$-based organic additives: there is a less pronounced shift and signal broadening when $SbCl_3$ interacts with TOP due to a less favored interaction compared to $InCl_3$. c) TOP: $InCl_3$ and $SbCl_3$ organic additives. A significant broadening and downfield shift in the TOP signal is observed due to the formation of TOP-$InCl_3$ complexes. After the formation and purification of InSb CQDs, there is no TOP leftover on the surface (bottom purple trace). d) TPP: $InCl_3$ and $SbCl_3$ organic additives. There is a minimal upfield shift in the TPP signal but no broadening, suggesting that the complexation to $InCl_3$ is frustrated due to steric constraints. e) Cartoon depicting the proposed reactivity mechanism between phosphines and $InCl_3$.

precursor (Figure S5, Supporting Information, green trace). This indicates the formation of a formal complex between OLAm and $SbCl_3$. Upon alane injection, the TOP signal sharpened and returned to its original position (Figure 1b), while the α-H signal remained broad, possibly due to the formation of a complex between OLAm and aluminum from the alane. Overall, isolated studies on the antimony precursor demonstrate a preference for $SbCl_3$ to interact with OLAm over TOP when both organics are present.

To gain direct insight into the formation mechanism of InSb CQDs, we repeated these experiments with both $InCl_3$ and $SbCl_3$ in the presence of TOP and OLAm. The ^{31}P NMR spectra clearly showed the broad signature of the TOP-$InCl_3$ complex before the addition of $SbCl_3$ (Figure 1c). Following the addition of $SbCl_3$, we see a negligible difference in the TOP signal because $SbCl_3$ forms a complex with OLAm as seen by the broadening of the α-H in the ^{1}H NMR spectrum (Figure S5c, Supporting Information), correlating with our individual experiments (Figure 1a). Notably, the addition of alane provokes a further broadening and downfield shift in the TOP signal (Figure 1c). We explain these observations by considering that at this moment in the reaction, InSb CQDs are formed, and TOP can interact with the QD surface, which will provoke homogeneous broadening in the NMR signals.[14,15] Finally, we do not observe any phosphorous signals in the purified InSb CQDs, which is clear evidence that TOP does not strongly bind the surface (Figure S7, Supporting Information).

In contrast, the control experiment with TPP shows no significant changes in the ^{31}P NMR signal shape and breath (Figure 1d). This suggests that the complexation of the $InCl_3$ is inhibited by steric hindrance. We also observe a shift in the signal, but this time it is an upfield shift. This does not correlate with a complexation to In^{3+} in which we would expect a downfield shift. We observe circumstantial evidence for the weak complexation of $InCl_3$

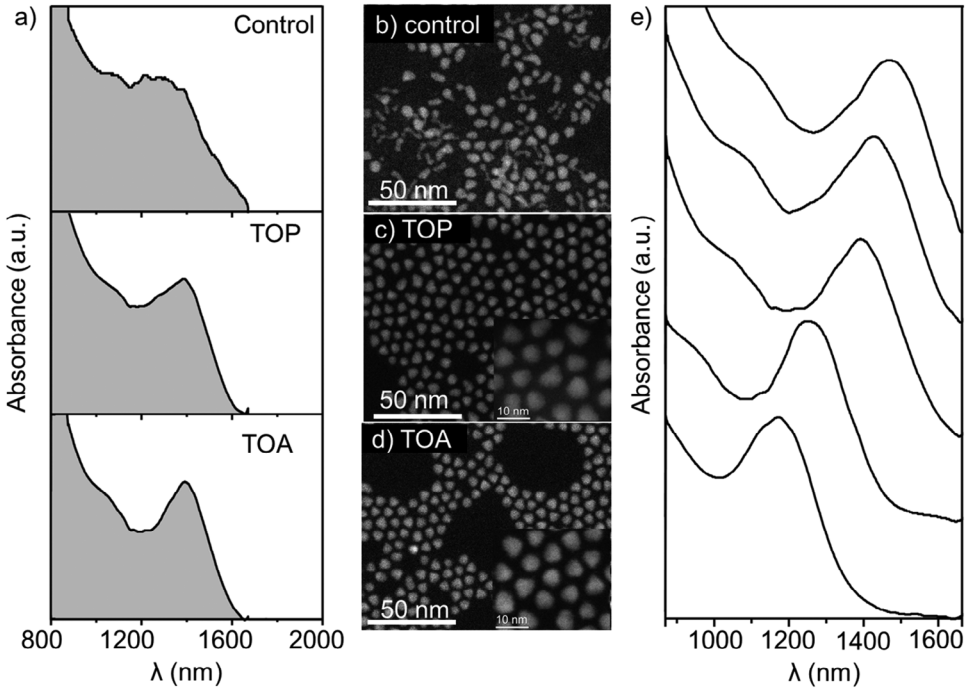

Figure 2. Additive-assisted growth of InSb CQDs. a) Optical absorption spectra InSb CQDs samples prepared without (control) and with different organic additives in solution. b–d) High angle annular dark field scanning transmission electron microscopy images (HAADF-STEM) analysis of InSb CQDs samples prepared (b) without, and (c-d) with organic additives. e) Size-dependent absorption spectra of InSb CQDs prepared using organic additives.

and OLA instead (Figure S8, Supporting Information). Figure 1e summarizes our observations regarding the interactions of phosphines with $InCl_3$.

Taken together, these results demonstrate that each of TOP and OLAm plays a key, yet distinctive, role in complexing the precursor salts. $InCl_3$ prefers to complex with TOP while $SbCl_3$ forms a complex with OLAm. This effect in precursor reactivity could explain why InSb reactions that avoid the use of both amines and phosphines translate into reactions that are not able to attain size control.

After confirming the formation of organic additive-metal halide adducts, we performed the synthesis of InSb CQDs with OLAm and TOP and compared them to a control sample in the absence of TOP. CQDs prepared using TOP and OLAm exhibited well-defined excitonic absorption peaks at 1410 nm and photoluminescence (PL) with narrow emission linewidths compared to the control sample (**Figure 2**a; Figure S9, Supporting Information) and PL quantum yield of 2–3%. HAADF-STEM analysis of InSb CQDs synthesized with OLAm and TOP revealed uniform shapes and narrow size distributions (Figure 2a; Figure S10, Supporting Information), while poor size control was identified in the control sample (Figure 2a,b). Then, we decided to test an additional additive in our reaction scheme, trioctylamine (TOA), to enhance the optical properties of InSb CQDs. The addition of TOA led to an increased peak-to-valley ratio in the absorption spectrum, reaching 1.5, while maintaining a narrow size distribution (Figure 2a,d; Figures S11 and S12, Supporting Information). This is likely due to the increased reactivity of metal precursors as observed previously in various materials systems.[18–21] PL measurements revealed a Stokes shift of ≈49 meV and a peak centered at 1490 nm (Figure S13, Supporting Information). Powder X-ray diffraction (PXRD) evidence the formation of phase-pure zinc blende InSb CQDs, with (111) plane being the most prominent (Figure S14, Supporting Information) in both TOP and TOA cases. We tested the effect of reaction temperature, heating ramp, and reducing agent to SbCl3 concentration in our optimized synthesis scheme, see details in Figures S15–S17 (Supporting Information).

We aimed to integrate OLAm-capped InSb CQDs from our optimized reaction scheme into photodiode devices by performing ligand exchange reactions. However, we found that the solid-state ligand exchange process – necessary to create conductive films – resulted in cloudy and inhomogeneous films (Figure S18, Supporting Information). Through X-ray photoelectron spectroscopy (XPS) analysis, we found that as-synthesized InSb CQDs show the presence of In_2O_3 and Sb_2O_x species as well as a strong O 1s peak (**Figure 3**a,b). Compositional analysis shows an In-to-Sb ratio of 1.51, indicating that the surface of the CQDs is indium that is highly oxidized. Since oxide species on the CQDs form trap states, we investigated ways to remove the oxides with an intermediate ligand treatment. We used density functional theory calculations to show that thiols can effectively remove surface oxides by donating a proton to OH groups. Based on this, we performed an in-solution dodecanethiol (DDT) treatment of the CQDs (Figure S19, Supporting Information, and see detailed discussion in Note S1, Supporting Information). XPS analysis showed that this process resulted in a decreased In:Sb ratio from 1.51 to 1.02 upon thiol exchange, indicating the effective removal of loosely bound excess Z-type $InCl_3$, and a significant reduction of oxide species (Figure 3a).

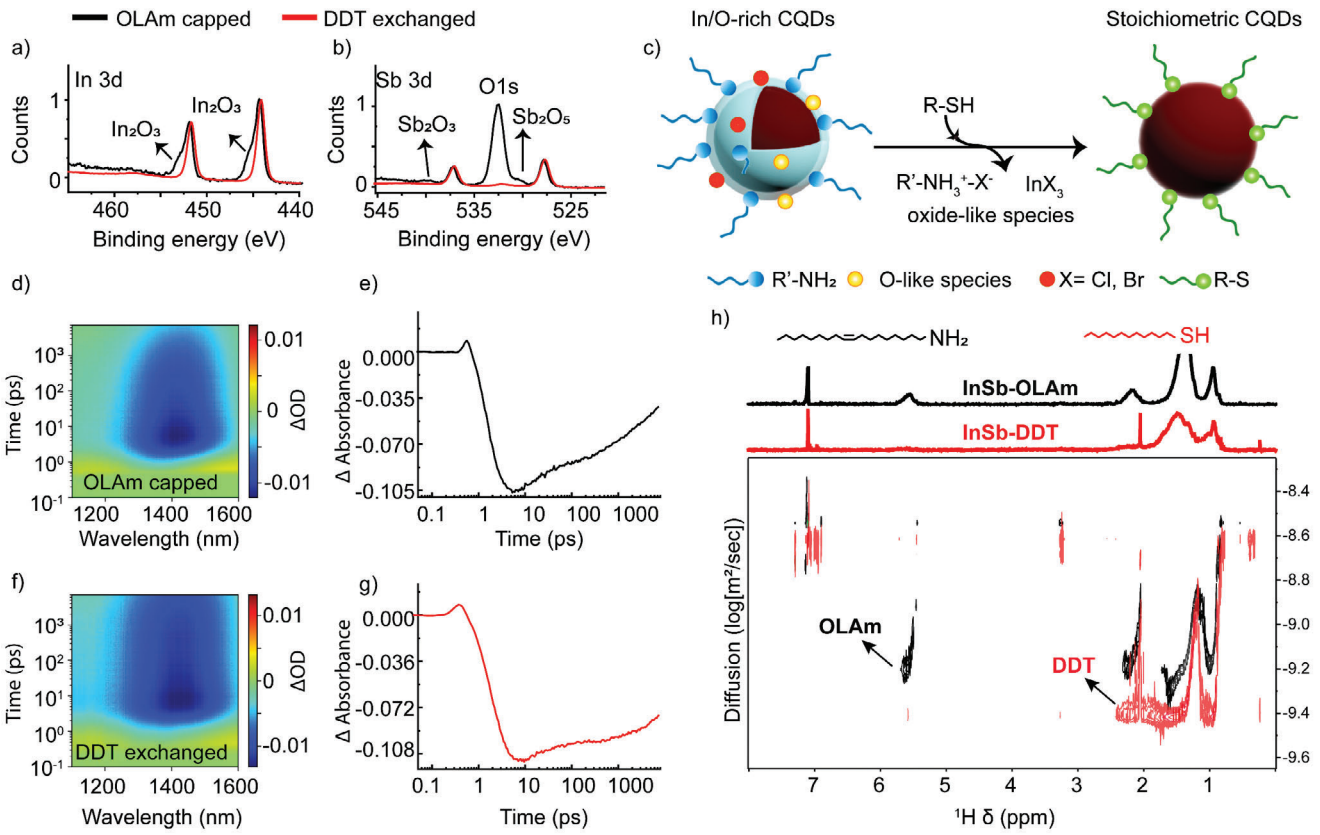

Figure 3. In-solution resurfacing of InSb CQDs. a,c) XPS analysis of as-synthesized (OLAm capped) and dodecanethiol (DDT) exchanged InSb CQDs. b) DOSY spectra for OLAm-capped InSb QDs purified through a regular workup (green trace) and those exchanged by DDT (purple trace). d) Schematic illustration of InSb CQDs resurfacing using alkanethiols. Transient absorption maps and bleaches of (e,g) OLAm capped, (f,h) and DDT exchanged CQDs.

We measured the transient absorption of OLAm- and DDT-capped InSb CQDs to study how different passivation affects carrier dynamics (Figure 3d–g). Both samples showed a well-defined excitonic peak at 1400 nm that decayed over time, fitting to two exponential components: a fast one (≈25 ps) attributed to Auger recombination,[22–24] and a slower one (2–6 ns) linked to nonradiative and radiative band-edge recombination. The longer decay component was notably longer for DDT-treated CQDs. Transient photoluminescence (PL) measurements also revealed faster PL decay for OLAm-capped CQDs (10–23 ns nonradiative, 59–89 ns radiative), with DDT treatment resulting in longer PL lifetimes and a lower nonradiative component (slow/fast = 0.24 for DDT vs 0.93 for OLAm), Figure S20 (Supporting Information). This suggests that DDT treatment effectively passivates surface defects, leading to lower trap density, and a threefold increase in PL intensity.

We conducted NMR experiments to investigate the surface chemistry of thiol exchanges on InSb CQDs surfaces. We hypothesized that exposing OLAm-capped InSb CQDs to alkane thiols would release oleylammonium chloride and bind thiolate species to surface indium atoms.[9,16,17] To test this, we added DDT to OLAm-capped CQDs and monitored ligand-related signals via 1H NMR. Upon adding DDT, we observed new features in the olefinic signal at ≈5.55 ppm, indicating the transition of OLAm from bound to a free state, and a broad signal at ≈8.0 ppm, associated with oleylammonium formation (Figures S21 and S22, Supporting Information). The displacement of OLAm is explained by DDT deprotonation and the formation of an oleylammonium chloride ion-pair adduct. DOSY measurements showed an increase in solvodynamic diameter from 1.5 to 2.2 nm after thiol treatment. These results suggest that thiolate species bind more strongly to In^{3+} atoms than OLAm, making CQDs colloidal stable after extra purification cycles.

Using the optimized DDT-capped InSb CQDs, we fabricated CQD films with some modifications to our previously reported method.[10] We used tetrabutylammonium iodide (TBAI) and Ammonium iodide salts during ligand exchange reactions to obtain halide passivated InSb CQDs (See details in the Method section, Figure S23, Supporting Information). This process was repeated four times to achieve a desired thickness of 280 nm. Subsequently, the spin-coated film was annealed on a hot plate at 100 °C for 1 h. XPS analysis of the CQDs film shows clean In3d and Sb 3d peaks (Figure S24, Supporting Information). Comparing fourier transform infrared spectroscopy (FTIR) spectra (**Figure 4a**) of the CQDs films before and after exchanges reveals a substantial decrease in C—H resonances ≈2950 cm^{-1}, indicating the complete displacement of native ligands and resulting in halide-passivated CQDs. Ultraviolet photoelectron spectroscopy (UPS) results show that ammonium iodide addition adjusts the energy levels to favor carrier transfer (Figure 4b; Figure S25,

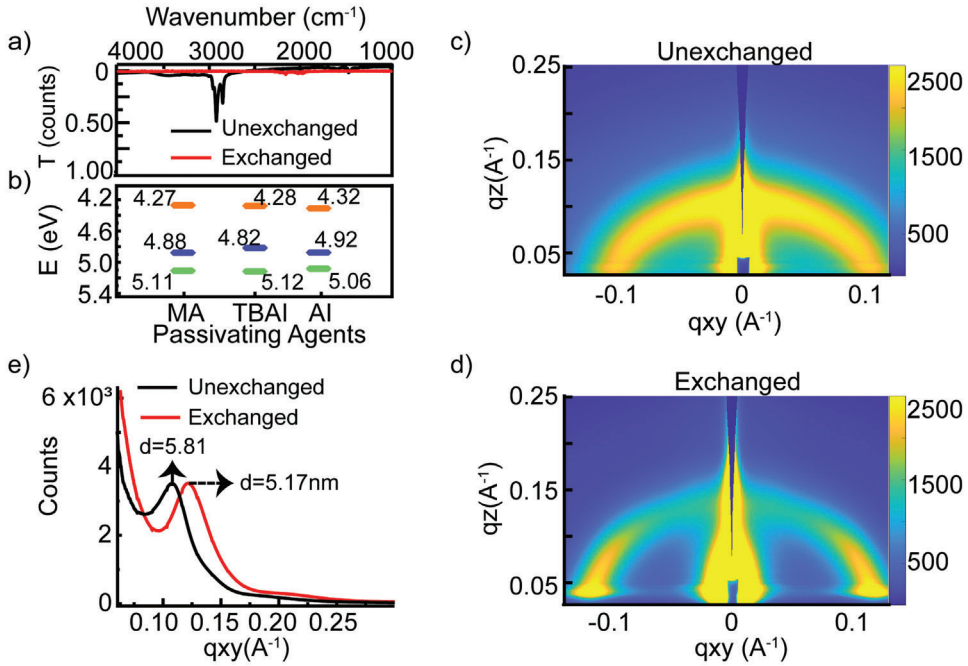

Figure 4. Unexchanged and exchanged CQD film characterization: a) FTIR analysis of unexchanged and exchanged CQD films. b) Ultraviolet photoelectron spectroscopy analysis of CQDs films after exchanges with different ligands. c,d) Grazing-incidence small-angle scattering (GISAX) pattern of (c) unexchanged and (d) exchanged CQDs films. e) Dot-to-dot ordering and distance of unexchanged and exchanged CQDs calculated from azimuthal integration of the GISAXS diffraction patterns.

Supporting Information). XRD analysis of the ligand-exchanged CQDs film shows retention of the native phase (Figure S26, Supporting Information).

Grazing-incidence small-angle scattering (GISAX) was used to examine the effect of ligand exchanges on the CQDs film. Control films were prepared using DDT-capped CQDs only and compared to those with ligand exchange. GISAXS patterns from unexchanged control and exchanged CQD films (Figure 4c,d) show an increase in diffraction intensity for the exchanged films. Azimuthal integration of GISAXS patterns reveals a sharper first-order peak centered at 0.106 Å for unexchanged QDs, which increases to 0.125 Å upon ligand exchanges. This corresponds to an average dot-to-dot distance for the unexchanged CQDs film of 5.81 nm, which decreases to 5.17 nm for exchanged CQDs (Figure 4e). The shorter dot-to-dot distance and increased peak-to-valley intensity of the azimuthal integration indicate that the CQDs are more closely packed in the exchanged sample.

We fabricated InSb CQDs photodiode devices using the *n-i-p* structure depicted in **Figure 5a**. Briefly, ZnO nanoparticles, which act as the electron transport layer, were deposited on an ITO substrate, followed by the deposition of ligand-exchanged InSb CQDs as described previously. Molybdenum oxide (MoO_x) was then thermally evaporated onto the InSb CQDs active layer. The structure was completed with Ag deposition to form the photodetector's top contact. Cross-sectional scanning electron microscopy (SEM) analysis of the devices revealed well-defined compositional layers (Figure 5b; Figure S27, Supporting Information). Figure 5c compares the dark current (J_{dark}) and light-dependent photoresponse of the InSb CQDs photodiode. The devices exhibited J_{dark} of ≈0.0144 mA cm^{-2} at 1 V reverse bias. Furthermore, the devices demonstrated a power-dependent response to 1450 nm light within the measurement range of 0.002–10.4 mW cm^{-2} (Figure 5c; Figure S28, Supporting Information), accompanied by a gradual increase in open-circuit voltage (V_{oc}). It also exhibited good rectification behavior with an impressive on-off ratio exceeding 10^3. This indicates that the photogenerated excitons directly contribute to the photocurrent, indicating that parasitic processes (e.g., carrier trapping and bimolecular recombination) are minimal. The devices showed an EQE of 10% at 0 V and 33% at 1 V (Figure 5d) with a thickness of 280 nm. Figure 5g shows responsivity R values of 0.35 A W^{-1} which is higher than those reported for devices in the same 1300–1500 nm wavelength range (see Table S1 and S2, Supporting Information).[11,25–27] Additionally, we obtained the spectral detectivity D^* using frequency-dependent noise current analysis (Figure 5e). As the frequency increased, we observed a linear decrease in device noise, surpassing the *1/f* noise region and reaching saturation at 2×10^3 Hz. The low noise level of 1.17×10^{-13} A Hz$^{-0.5}$ contributed to a high D^* of 10^{12} Jones at the excitonic peak (as shown in Figure 5f) under a 1 V bias.

We then investigated the photodetector's transient photocurrent responses (Figure 5g). The photodetector exhibited fall times (from 90% to 10% of the normalized photocurrent) of 2.3 and 1.4 µs at 0 and 1 V, respectively. We subsequently studied operating stability under 1450 nm laser light in a nitrogen environment (Figure 5h; Figure S29, Supporting Information). The InSb photodiode devices retained over 90% of their initial photocurrent after 19 h of continuous, biased (0.5 V) operation. To the best of our knowledge, this is the highest EQE and operating stability

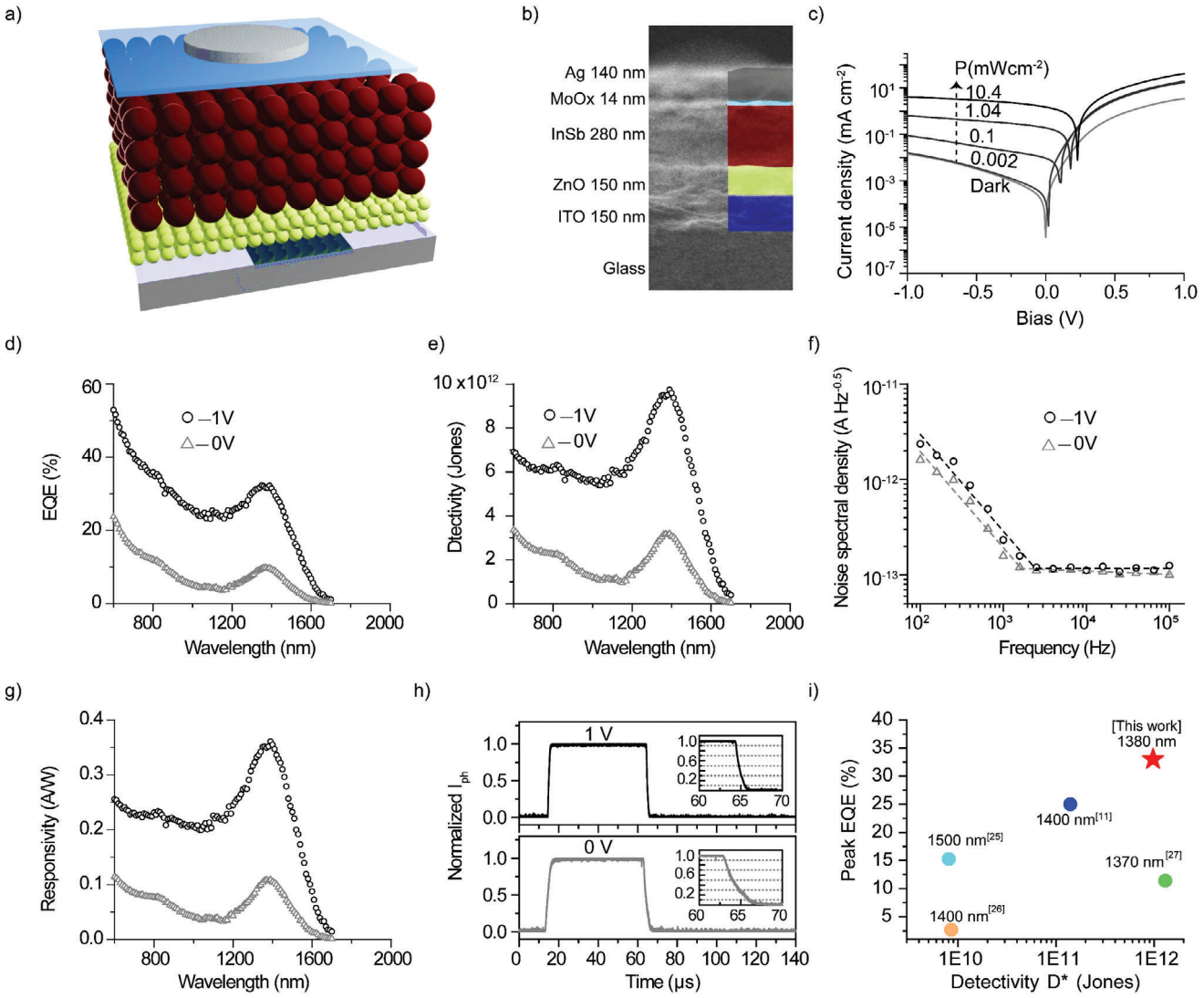

Figure 5. InSb CQD-based IR photodetector performance. a) Scheme showing the device architecture used in InSb photodiodes devices. b) Cross-sectional scanning electron microscopy image of the device stack. c) Dark and power-dependent illuminated *J–V* characteristics of InSb photodetector. d) EQE, e) detectivity, f) noise current, g) responsivity, h) and transient photocurrent at 0 and 1 V of InSb CQDs photodiodes devices. i) Comparison of the device performance with previous reports on III-V CQDs-based photodiodes.

reported among infrared III-V CQDs-based devices operating in the same wavelength range (1.3–1.5 µm).

3. Conclusion

In conclusion, using NMR spectroscopy, we designed an organic additives-metal halide model system. These organic additives form strong adducts with metal halide precursors, controlling their reactivity during nucleation and growth processes. This approach enabled the uniform synthesis of InSb CQDs. The synthesized CQDs are surface terminated with a mixture of alkylammonium halide and indium oxides, which inhibit ligand exchange reactions. Alkanethiols initiate ligand exchange, involving the binding of the conjugate base RX^- and the desorption of alkylammonium halide and indium oxides. This approach enabled us to fabricate a highly efficient InSb-based photodiode, achieving a detectivity of 10^{12} Jones, an external quantum efficiency (EQE) of 33% at 1380 nm, and improved operational stability, retaining 90% of their initial performance after 19 h of continuous illumination.

Supporting Information

Supporting Information is available from the Wiley Online Library or from the author.

Acknowledgements

M.I., D.B.K., and P.X. equally contributed to this work. The authors thank Larissa Levina, Elenita Palmiano, Remi Wolowiec, and Damir Kopilovic for their assistance during the period of study.

Conflict of Interest

The authors declare no conflict of interest.

Data Availability Statement

The data that support the findings of this study are available from the corresponding author upon reasonable request.

Keywords

colloidal quantum dots, group III-V semiconductors, indium antimonide, photodetector, short wave-infrared

Received: December 23, 2024
Revised: January 28, 2025
Published online:

[1] A. Rogalski, P. Martyniuk, M. Kopytko, P. Madejczyk, S. Krishna, *Sensors* **2020**, *20*, 7047.
[2] G. Konstantatos, E. H. Sargent, *Nat. Nanotechnol.* **2010**, *5*, 391.
[3] M. Liu, N. Yazdani, M. Yarema, M. Jansen, V. Wood, E. H. Sargent, *Nat. Electron.* **2021**, *4*, 548.
[4] M. Neathery, W. Miller, *J. Dairy Sci.* **1975**, *58*, 1767.
[5] W. Liu, A. Y. Chang, R. D. Schaller, D. V. Talapin, *J. Am. Chem. Soc.* **2012**, *134*, 20258.
[6] T. Zhao, N. Oh, D. Jishkariani, M. Zhang, H. Wang, N. Li, J. D. Lee, C. Zeng, M. Muduli, H.-J. Choi, D. Su, C. B. Murray, C. R. Kagan, *J. Am. Chem. Soc.* **2019**, *141*, 15145.
[7] Muhammad, D. Choi, D. H. Parmar, B. Rehl, Y. Zhang, O. Atan, G. Kim, P. Xia, J. M. Pina, M. Li, Y. Liu, O. Voznyy, S. Hoogland, E. H. Sargent, *Adv. Mater.* **2023**, *35*, 2306147.
[8] W. J. Mir, T. Sheikh, S. Nematulloev, P. Maity, K. E. Yorov, A.-H. Emwas, M. N. Hedhili, M. S. Khan, M. Abulikemu, O. F. Mohammed, O. M. Bakr, *Small* **2024**, *20*, 2306535.
[9] Y. Kwon, O. Yeromina, M. Cavallo, M. G. Silly, D. Pierucci, E. Lhuillier, D. Aldakov, B. Hyot, P. Reiss, *Adv. Funct. Mater.* **2024**, *34*, 2403912.
[10] J. Leemans, K. C. Dümbgen, M. M. Minjauw, Q. Zhao, A. Vantomme, I. Infante, C. Detavernier, Z. Hens, *J. Am. Chem. Soc.* **2021**, *143*, 4290.
[11] Y. Zhang, P. Xia, B. Rehl, D. H. Parmar, D. Choi, M. Imran, Y. Chen, Y. Liu, M. Vafaie, C. Li, O. Atan, J. M. Pina, W. Paritmongkol, L. Levina, O. Voznyy, S. Hoogland, E. H. Sargent, *Angew. Chem.* **2024**, *136*, 202316733.
[12] L. Peng, Y. Wang, Y. Ren, Z. Wang, P. Cao, G. Konstantatos, *ACS Nano* **2024**, *18*, 5113.
[13] J. J. Calvin, A. S. Brewer, A. P. Alivisatos, *Nat. Synth.* **2022**, *1*, 127.
[14] M. Vafaie, A. Morteza Najarian, J. Xu, L. J. Richter, R. Li, Y. Zhang, M. Imran, P. Xia, H. W. Ban, L. Levina, A. Singh, J. Meitzner, A. G. Pattantyus-Abraham, F. P. García de Arquer, E. H. Sargent, *Proc. Natl. Acad. Sci. USA* **2023**, *120*, 2305327120.
[15] H. W. Ban, M. Vafaie, L. Levina, P. Xia, M. Imran, Y. Liu, A. M. Najarian, E. H. Sargent, *J. Am. Chem. Soc.* **2024**, *146*, 24935.
[16] Z. Hens, J. C. Martins, *Chem. Mater.* **2013**, *25*, 1211.
[17] J. De Roo, N. Yazdani, E. Drijvers, A. Lauria, J. Maes, J. S. Owen, I. Van Driessche, M. Niederberger, V. Wood, J. C. Martins, I. Infante, Z. Hens, *Chem. Mater.* **2018**, *30*, 5485.
[18] Y. H. Kim, Y. W. Jun, B. H. Jun, S. M. Lee, J. Cheon, *J. Am. Chem. Soc.* **2002**, *124*, 13656.
[19] S. Xu, S. Kumar, T. Nann, *J. Am. Chem. Soc.* **2006**, *128*.
[20] M. Imran, W. Paritmongkol, H. A. Mills, Y. Hassan, T. Zhu, Y.-K. Wang, Y. Liu, H. Wan, S. M. Park, E. Jung, J. Tam, Q. Lyu, G. F. Cotella, P. Ijaz, P. Chun, S. Hoogland, *Adv. Mater.* **2023**, *35*, 2303528.
[21] Z. Liu, R. Pascazio, L. Goldoni, D. Maggioni, D. Zhu, Y. P. Ivanov, G. Divitini, J. L. Camarelles, H. B. Jalali, I. Infante, L. De Trizio, L. Manna, *J. Am. Chem. Soc.* **2023**, *145*, 18329.
[22] V. Klimov, A. Mikhailovsky, D. McBranch, *Science* **2000**, *287*, 1011.
[23] G. Nootz, L. A. Padilha, L. Levina, V. Sukhovatkin, S. Webster, L. Brzozowski, E. H. Sargent, D. J. Hagan, E. W. Van Stryland, *Phys. Rev. B—Condensed Matter Mater. Phys.* **2011**, *83*, 155302.
[24] R. J. Ellingson, M. C. Beard, J. C. Johnson, P. Yu, O. I. Micic, A. J. Nozik, A. Shabaev, A. L. Efros, *Nano Lett.* **2005**, *5*, 865.
[25] T. Sheikh, W. J. Mir, A. Alofi, M. Skoroterski, R. Zhou, S. Nematulloev, M. N. Hedhili, M. B. Hassine, M. S. Khan, K. E. Yorov, B. E. Hasanov, H. Liao, Y. Yang, A. Shamim, M. Abulikemu, O. F. Mohammed, O. M. Bakr, *J. Am. Chem. Soc.* **2024**, *146*, 29094.
[26] J. Leemans, V. Pejovic, E. Georgitzikis, M. Minjauw, A. B. Siddik, Y.-H. Deng, Y. Kuang, G. Roelkens, C. Detavernier, I. Lieberman, P. E. Malinowski, D. Cheyns, Z. Hens, *Adv. Sci.* **2022**, *9*, 2200844.
[27] H. Seo, H. J. Eun, A. Y. Lee, H. K. Lee, J. H. Kim, S. W. Kim, *Adv. Sci.* **2024**, *11*, 2306439.